



**HAL**  
open science

# Pellet core fueling in tokamaks, stellarators and reversed field pinches

E. Geulin, B. Pégourié

► **To cite this version:**

E. Geulin, B. Pégourié. Pellet core fueling in tokamaks, stellarators and reversed field pinches. ITC30 - The 30th International Toki conference on plasma and fusion research, Nov 2021, E-conference, France. cea-03520622

**HAL Id: cea-03520622**

**<https://cea.hal.science/cea-03520622>**

Submitted on 11 Jan 2022

**HAL** is a multi-disciplinary open access archive for the deposit and dissemination of scientific research documents, whether they are published or not. The documents may come from teaching and research institutions in France or abroad, or from public or private research centers.

L'archive ouverte pluridisciplinaire **HAL**, est destinée au dépôt et à la diffusion de documents scientifiques de niveau recherche, publiés ou non, émanant des établissements d'enseignement et de recherche français ou étrangers, des laboratoires publics ou privés.

# Pellet core fueling in tokamaks, stellarators and reversed field pinches

E. Geulin<sup>1</sup> and B. Pégourié<sup>1</sup>

<sup>1</sup>CEA, IRFM, 1508 Saint-Paul-Lez-Durance, France

[eleonore.geulin@cea.fr](mailto:eleonore.geulin@cea.fr)

## Abstract

In a reactor grade device, the role of core fueling is to replace the D and T consumed in the fusion reactions (almost negligible) and to compensate the plasma losses through the separatrix - including the material expelled out by the ELMs. For this purpose, deep material deposition is an advantage and pellet injection the best candidate for fueling the future machines. Fueling by pellet injection consists in two phases: First, the pellet ablation itself, then the ablated material homogenization and drift in the discharge. The former is a self-regulated process, which depends only of the local plasma characteristics. The second is a global phenomenon, which depends on the whole magnetic configuration. In this presentation, we discuss first the basics of the ablation physics, emphasizing the role of the fast particles – ions and electrons – resulting from NBI or wave heating; then we describe the homogenization process and associated  $\nabla B$ -induced drift. The drift acceleration and damping processes are described as well as the influence of the magnetic configuration (tokamak, stellarator and reversed field pinch) on the predominance of a given damping process and its consequence on the resulting deposition profile. We finally review the last results relative to pellet fueling in these different kind of devices and present the ongoing projects for future large-scale machines.

# 1 Introduction

In a fusion reactor, the role of core fueling is (1) to replace the DT consumed in fusion reactions, (2) to compensate the gas exhausted with the Helium ashes and (3), to maintain the central density by compensating the particle outflux across the separatrix (which depends on the transport regime and on the density gradient at the edge).

The amount of fuel consumed in fusion reactions is generally negligible:  $3.55 \cdot 10^{20}$  D and T/GW, i.e.  $1.5 \text{ Pa}\cdot\text{m}^3 \text{ D}_2+\text{T}_2/\text{GW}$ . The quantity to be injected for replacing the gas exhausted with the ashes depends on the maximum acceptable concentration of Helium in the core for maintaining a high enough reactivity. Considering a conservative value  $n_{\text{He}}/n_e \sim 8\%$ , one should inject  $3.7 \cdot 10^{21}$  D+T/GW, i.e.  $7.8 \text{ Pa}\cdot\text{m}^3 \text{ D}_2+\text{T}_2/\text{GW}$ . The most important contribution comes from the conservation of the core density. Taking as an example an ITER-like device, with a major radius of 6 m, a minor radius of 2 m and an elongation 1.7, with a density gradient in the pedestal of  $\sim 3 \cdot 10^{20} \text{ m}^{-4}$  and using an effective value for the diffusion coefficient of  $0.1 \text{ m}^2/\text{s}$ , one obtains an integrated outflux of  $\sim 2.5 \cdot 10^{22} \text{ e}_-/\text{s}$  which requires – to be compensated – an injection of  $\sim 50 \text{ Pa}\cdot\text{m}^3/\text{s}$  of  $\text{D}_2+\text{T}_2$ . It is to be noted that these contributions are not strictly additive (the Helium flux is included in that resulting from the edge density gradient).

Due to the width and density / temperature of the Scrape-Off Layer (SOL) in a large-scale device, the screening of the neutrals is important and a simple gas injection from the edge is not efficient enough for feeding the plasma at the required level [1]. Direct fuel injection inside the separatrix, even beyond the top of the pedestal, is mandatory for reaching the required core density. Moreover, this fueling should be ideally done at low energetic cost and without injecting any power or momentum in the discharge. Despite a deep penetration, Neutral Beam Injection (NBI) cannot be used for fueling, on one hand because it couples particle and power injections, on the other hand because the corresponding fluxes ( $\sim 6 \cdot 10^{21}$  at. MW/keV, i.e.  $\sim 1 \text{ Pa}\cdot\text{m}^3/\text{s}$  for 73 MW injected with 1 MeV neutrals in ITER) are well

below the required values. A second option is the injection of cryogenic pellets, a widely documented and mature technique, from both the points of view of the physics ([2], [3]) and of the technical developments [4]. In the future, injection of compact toroids is also envisaged [5], but this technique is not yet developed enough for it to be used in the machines for which beginning of operation is planned during the next decade.

This paper presents the physics of fueling by pellet injection, summarizes the main results obtained in this field during the last decade, and describes the injectors and injection lines presently under manufacturing or planned for the next generation devices. Practically, a simple description of the physics of the pellet ablation and of the homogenization of the deposited material is given in Sections 2 and 3, explicating the contributions of the different mechanisms at work in tokamaks, stellarators and Reversed Field Pinches (RFPs), and discussing how their respective weight influence the final shape of the matter deposition profile. The main results recently obtained on the tokamaks and stellarators in operation – all of them relative to the compatibility of pellet injection with high performance scenarios - are reviewed in Section 4, and the pellet fueling systems planned in the next step (JT-60SA, ITER) or future (JA/EU-DEMO, FFHR) devices are briefly described in Section 5. Finally, the most important points are summarized in Section 6.

## 2 Physics of ablation

As soon as a pellet enters into the plasma, the incident ion and electron heat fluxes vaporize its external layers. This ablated material surrounds the pellet and – as long as its ionization degree remains low - stays attached to the pellet in its motion through the plasma. The cold and dense vapor layer absorbs the quasi-totality of the plasma heat flux, protecting the pellet and allowing a deep penetration inside the discharge, much larger than what would be the penetration of gas. In a first approximation, it is a self-regulated process, which only depends on the pellet size and local plasma characteristics (density, temperature and

magnetic field): the ablation cloud self-adapts such that the heat flux reaching the pellet is just enough for the newly ablated material to replace the material loss due to the progressive ionization. Three mechanisms participate to the cloud protection, by order of increasing efficiency they are : the cloud diamagnetism, which reduces the effective area of the plasma flux tube intercepted by the cloud, the electrostatic sheath that develops at the plasma cloud interface and repels a part of the incident electrons, and finally the Coulomb collisions inside the cloud (Fig. 1). If

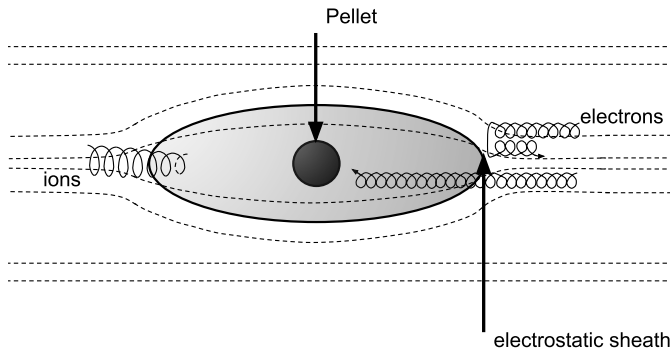


Figure 1: Schematic picture of an ablation cloud showing the local distortion of the magnetic field due to the cloud diamagnetism (magnetic shielding), the sheath at the two ends (the cloud is negatively charged, electrostatic shielding), and the electron and ions stopped at various depths inside the cloud (collisional shielding).

the electrostatic sheath does not change the total heat flux on the cloud, by repelling the electrons and accelerating the ions, it causes a power transfer from the former to the latter. The stopping cross-section of the ions with the cloud particles being larger than that of the electrons (see Fig. 2), the ion heat flux is absorbed at the cloud periphery and only a reduced electron heat flux penetrates deep inside the cloud and ablates the pellet. The most efficient shielding is by far the Coulomb stopping, by which the quasi-totality of the remaining heat flux is absorbed through collisions with the cloud particles, and it is enough to consider this latter shielding for deriving the main dependence of the pellet ablation rate with pellet size and plasma temperature and density.

The so-called Neutral Gas Shielding (NGS)

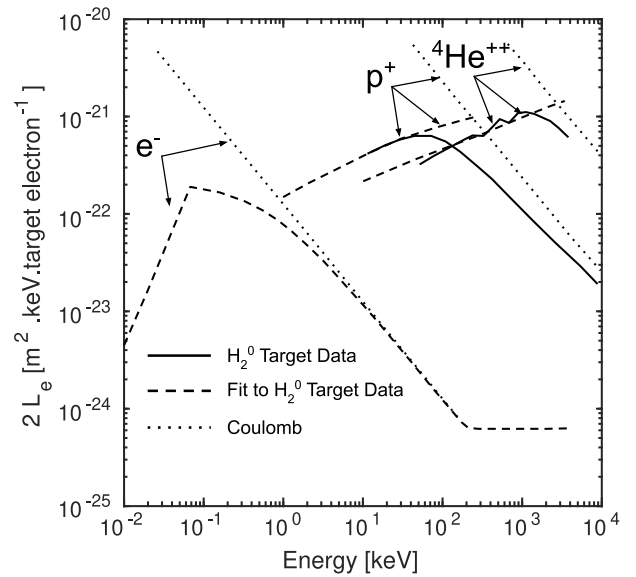


Figure 2: Stopping cross-sections for electrons, hydrogenic ions, and Helium ions. Solid curves represent experimental data for stopping in Hydrogen gas, long-dashed curves are fits to the experimental data, and short-dashed curves are theoretical values for Coulomb stopping in a cold electron plasma [6].

scaling is easily deduced from the matter and energy conservation at the pellet / cloud and cloud / plasma interfaces. Main assumption is that the incident electrons loose their whole energy  $E_\infty$  by collisions inside the cloud of density  $n_0$  (the sublimation energy of Hydrogen is small enough to be neglected in a first approximation). Every electron losing its energy with a rate  $dE/ds \propto n_0 E^{-2/3}$  along the distance  $s$  covered inside the cloud (dotted line in Fig. 2), the amount of matter required for stopping the electrons can be written  $n_0 s \propto E_\infty^{5/3}$  (it is assumed that the cloud size is proportional to that of the pellet:  $s \propto r_p$ , where  $r_p$  is the pellet radius). At steady state, the particle and energy fluxes must be conserved across the pellet / cloud and cloud / plasma interfaces, which writes:

$$\begin{aligned} n_p r_p &\sim n_0 T_0^{1/2} \\ n_\infty E_\infty^{3/2} &\sim n_0 T_0^{3/2} \end{aligned}$$

where  $n_p$  is the Hydrogen ice density and  $n_\infty$  that of the plasma. Combining these relations, one

obtains:

$$r_p \sim \frac{1}{n_p} \left[ \frac{n_\infty E_\infty^5}{r_p^2} \right]^{1/3} \quad (1)$$

Despite the numerous approximations, this scaling was confirmed for Maxwellian plasmas by more sophisticated models taking into account the other shielding mechanisms and was validated over a large number of experiments in several machines ([2], [3] and references therein, [7], [8]). Reasons for this robustness are detailed in [9]. One observes nevertheless large deviations to this ablation law as soon as the electron or ion distribution functions exhibit significant suprathermal tails. In the presence of fast ions (Ion Cyclotron Resonance Heating (ICRH) or Neutral Beam Injection (NBI))<sup>1</sup>, overablation is due to a geometrical effect. The ion orbit dimensions becoming comparable to those of the cloud, the fast ions can enter laterally and reach the pellet after having only covered a short distance inside the shielding cloud, which increases the residual heat flux at the pellet surface, and thus the ablation rate. Several models were developed for quantifying this overablation ([6], [10], [11]) and their predictions compared with experiments performed in tokamaks or stellarators with ICRH [11] or NBI additional power ([10], [12], [13]). The situation is different in the presence of fast electrons, for which the stopping cross-section becomes weak enough for they can cross the cloud and even the pellet without being stopped (see Fig. 2). A volume heating of the pellet follows, which entirely vaporizes when the amount of accumulated heat becomes comparable to the sublimation energy of the whole material contained in the pellet. Practically, this situation is met in tokamak discharges where Lower Hybrid Current Drive (LHCD) generates the current in a non-inductive way [11] or in the presence of a beam of runaway electrons. Electron Cyclotron Resonance Heating (ECRH) does not generate a significant suprathermal tail, but this method allows a localized power deposition, which can also lead to a local overablation [14].

<sup>1</sup>In a reactor, the  $\alpha$ -particles are not expected to have a significant effect because the pellet will be fully ablated in the external part of the plasma

### 3 Physics of homogenization

As the pellet is ablated, it leaves along its path a series of dense and cold cloudlets (radius  $\sim 1$  cm, length  $\sim 10$  cm, typically  $1000\times$  denser and colder than the background plasma). These cloudlets homogenize in the discharge by expanding along the field lines (see e.g. [15]). Nevertheless, since the parallel energy transport ( $\sim$  at the thermal electron velocity) is much faster than the density parallel transport ( $\sim$  at the sound velocity), the temperatures in the cloudlet and the background plasma equilibrate much faster than the densities, leading to a localized overpressure in the cloudlet. A charge separation develops then in the cloud, due to the vertical drift of electrons and ions ( $v_{\nabla B e/i}$ ) in the inhomogeneous magnetic field  $B_\infty$ . The associated current,  $\delta j_{\nabla B}$ , is compensated by a polarization current,  $j_{pol}$ , driven by an electric field  $E$ , which induces a  $E \times B_\infty$  drift down the magnetic field gradient (Fig. 3). This drift velocity writes ([16], [17], see a more complete discussion in [2]):

$$\frac{dV_d}{dt} = \left[ \frac{dV_d}{dt} \right]_{\nabla B} = \frac{2(n_0 T_0 (1 + M_0^2/2) - n_\infty T_\infty)}{R_c n_0 m_0} \quad (2)$$

where  $T_\infty$  is the temperature of the background plasma and where  $T_0$ ,  $m_0$  and  $M_0$  are the temperature, the ion / atom mass and the Mach number of parallel expansion in the cloudlet (the parallel expansion increases the electron and ion vertical curvature drift and thus the cloudlet polarization).  $R_c$  is the curvature radius of the magnetic field lines ( $\sim$  the major radius in a tokamak). At the beginning of the drift, during the phase of ideal MHD, the cloudlet drags away the magnetic flux tube it intercepts: the potential distribution propagates along the flux tube, from the two ends of the cloudlet, carried by an Alfvén wave at velocity  $C_A$  (Alfvén velocity). This mechanism is schematized in Fig. 4, showing that, due to the magnetic tension, the field exerts a force per surface unit,  $F_m = B_\infty^2 / \mu_0$  that, projected on the direction of the cloudlet displacement, generates a return force that brakes the drift (see e.g. [18]). The equation for the evolution of the drift veloc-

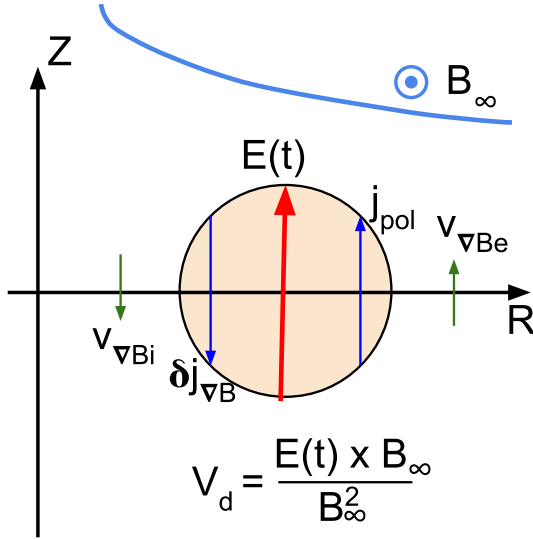


Figure 3: Simple description of cloud acceleration down the field gradient in an inhomogeneous magnetic field.

ity writes then:

$$\frac{dV_d}{dt} = \left[ \frac{dV_d}{dt} \right]_{\nabla B} - V_d \frac{2B_\infty^2}{\mu_0 C_A n_0 m_0 Z_0} \quad (3)$$

Where  $Z_0$  is the cloudlet parallel length. As long as the only two terms of the r.h.s. of Eq.3 are considered, the cloudlet drift stops a short time after pressure equilibration (which implies also that the cloudlet parallel expansion stops) and the specificities of the different magnetic configurations (tokamak, stellarator or RFP) do not play any role. With increasing time, the cloudlet

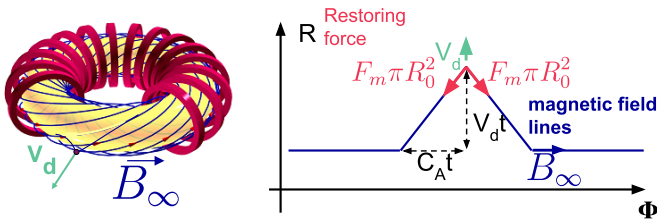


Figure 4: Simple description of drift braking by Alfvén wave emission ( $\Phi$  is the parallel direction).

electric potential perturbation invades the whole magnetic surface and the cloudlet length, that increases typically at the sound speed,  $C_s(T_0)$ , becomes large enough for covering significant poloidal and toroidal angular sectors. This situation is the source of two processes that contribute simultaneously to the damping of the cloudlet drift, more

efficiently than the Alfvén damping.

The former (External Connection, EC) results from the connection along the same flux tube of two regions oppositely charged (Fig .5). The circuit is then closed by a resistive parallel current,  $j_{||}$ , along this flux tube, the cloudlet acting as a current generator. In this regime, the damping term due to the Alfvén wave emission vanishes progressively, and the equation of evolution of the drift velocity writes ([19]):

$$\frac{dV_d}{dt} = \left[ \frac{dV_d}{dt} \right]_{\nabla B} - V_d \frac{\sigma_\infty B_\infty^2 \pi R_0^2}{2n_0 m_0 Z_0 Z_\infty} \quad (4)$$

where  $\sigma_\infty$  is the plasma parallel conductivity and  $Z_\infty$  the length of the flux tube connecting the two ends of the cloudlet. On the major part of the discharge,  $Z_\infty$  is bounded by  $2\pi^2 R a / R_0$ , where  $R$  and  $a$  are the major and minor radii of the plasma, but it decreases down to  $2\pi q R$ , where  $q$  is the safety factor, close to the integer rational surfaces that play a preponderant role in the stopping of the drift.

The second (Internal Connection, IC) results

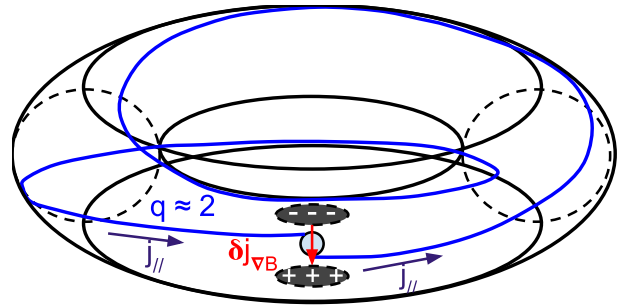


Figure 5: Drift damping by external connection in a tokamak (the situation is essentially the same in a stellarator) [3]

from the progressive misalignment of the current  $\delta j_{\nabla B}$  as the cloudlet, whose parallel length increases continuously, covers wider and wider poloidal and toroidal angular sectors [20]. Beyond a critical length  $Z_c$ , the relative directions of the current  $\delta j_{\nabla B}$  are inverted at the two cloudlet ends (w.r.t. the field lines), and the circuit is closed by a parallel current inside the cloudlet, Fig.6. This second phenomenon does not brake the drift, but decreases drastically its driving term. Its integration in the equation of evolution of the drift

velocity leads to (see e.g. [21]):

$$\frac{dV_d}{dt} = \left[ \frac{dV_d}{dt} \right]_{\nabla B} \frac{Z_c}{\pi Z_0} \sin \left( \frac{\pi Z_0}{Z_c} \right) \quad (5)$$

It is the fact that these two last mechanisms de-

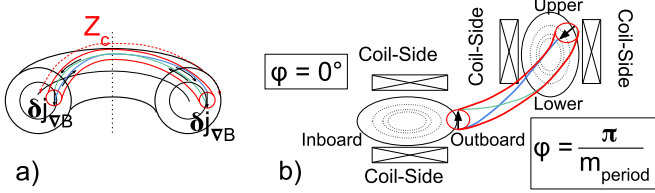


Figure 6: Drift damping by internal connection in a tokamak (a) and in a stellarator (b). Blue and green lines represent two magnetic field lines along which parallel currents flow. Black arrows are the curvature and gradient currents inside the cloud ([20, 21])

pend on the magnetic configuration that determines the drift dynamics in the different kinds of devices (tokamak, stellarator or RFP) and thus the resulting matter deposition profile. See also [22] for MHD simulations.

In tokamaks, the time after which the EC becomes efficient scales as  $\tau_{EC} \sim \frac{2\pi R}{C_A}$  close to the strongly rational surfaces (Fig.5), shorter than that after which the IC becomes efficient  $\tau_{IC} \sim \frac{\pi q R}{C_s(T_0)}$ , Fig.6a. It is therefore this former process that is dominant in the stopping of the drift and the matter deposition profile exhibits a stair-like shape (the deposition peak progresses step by step with pellet ablation), every integer or half-integer surface acting as a drift barrier (Fig.7, [23]). Conversely, in stellarators, if the time  $\tau_{EC}$  is of the same order of magnitude as in tokamaks, the length  $Z_c$  beyond which the IC becomes efficient is only half the toroidal period of the configuration,  $Z_c \sim \frac{\pi R}{m_{\text{period}}}$ , where  $m_{\text{period}}$  is the number of periods [21], Fig 6b. Consequently,  $\tau_{IC} < \tau_{EC}$ , and the drift stopping in stellarators is dominated by the IC. In helical devices, the  $\nabla B$  induced displacement is – for machines of similar size and plasma conditions – smaller than in tokamaks.

In RFPs, the poloidal magnetic field is larger than the toroidal magnetic field in the external half of the plasma, where the major part of ablation occurs, Fig.8. The drift is then essentially directed

outwards, along the minor radius. The cloudlet homogenization time (pressure equilibration) is short, because of the large magnetic shear that strongly stretches the cloudlets during their parallel expansion, increasing their cross-field surface, and of the large transport coefficients in these devices [24]. At the reversal radius, where the toroidal field vanishes and changes direction, the connection length  $Z_\infty$  is very short,  $\sim 2\pi a$ . Locally, the damping of the drift is very efficient and the material deposited at this place takes the shape of an overdense poloidal ring that expands in the toroidal direction more slowly than the matter deposited deeper in the discharge [24]. The model described above was implemented in different codes adapted to the tokamak configuration<sup>2</sup> or to the stellarators ([21, 27]) and checked against experiments over a significant number of devices ([2, 3] and references therein, [21, 28, 29, 30, 31]).

## 4 Recent results in fueling

The deep matter penetration in a discharge fueled by pellet injection has two main advantages: a higher fueling efficiency ( $\epsilon_f$ , defined as the proportion of injected particles present in the plasma at the end of injection) and a wider operational domain in density, because of a better decoupling between the core and edge plasma densities. These two facts are documented for a long time in the literature (see [2] and references therein) and only the most salient points and recent results are listed below.

In tokamaks, if one excepts the injection of energetic neutrals – which couples a significant power injection to a modest fueling, and the injection of compact toroids – for which technology is not mature enough, the injection of cryogenic pellets is the fueling method exhibiting the highest efficiency (with  $\epsilon_f(GP) < 10\%$  for a gas puffing,  $\epsilon_f(SMBI) \sim 30$  to 60% for Supersonic Molecular Beam Injection [32] and  $\epsilon_f(PI) \sim 30$  to 90% for pellet injection). In the case of pellet injection

<sup>2</sup>A pure MHD description of the drift and of the resulting modification of the deposition profile is found in [25, 26]

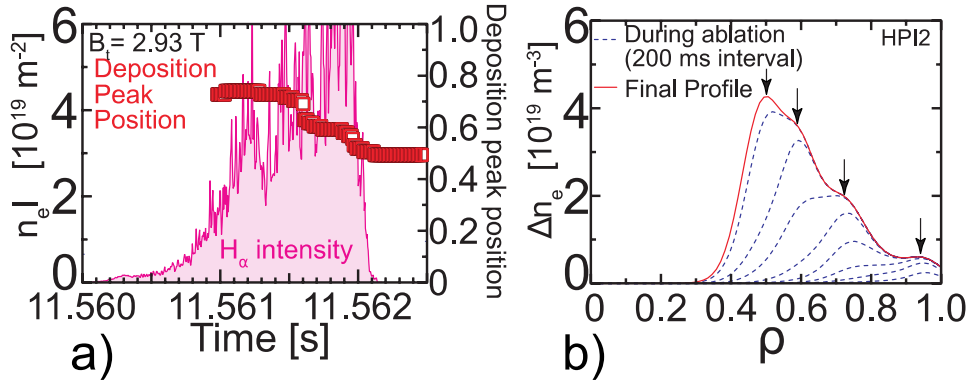


Figure 7: (a) Time evolution of the deposition peak position (squares) and ablation light emission (thin line, shadowed region) during a pellet injection in Tore Supra. (b) Time evolution of the calculated pellet deposition profile ( $\rho = r/a$ ). The arrows denote the position of the deposition peaks whose sum forms the deposition profile [23].

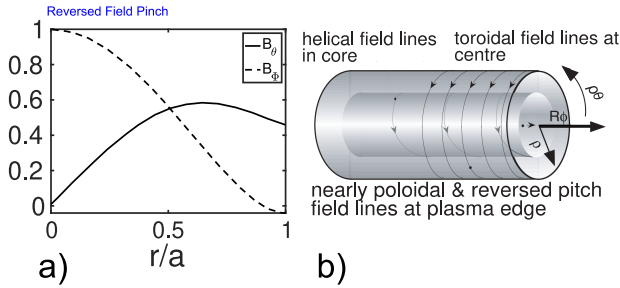


Figure 8: Magnetic configuration of a RFP. (a)  $B_\infty$ -field component profiles. (b) The drift damping by external connection is particularly efficient close to the reversal radius, where field lines are nearly poloidal [24].

tion, the wide range in  $\epsilon_f$  and deposition depth comes from the variable contribution of the  $\nabla B$ -induced drift to the matter penetration ([2], [33], see Fig. 9). This is the reason why, in most experiments, pellets are injected from the High Field Side (HFS) of the machine, and not from its Low Field Side (LFS).

Nevertheless, the good instantaneous fuelling properties demonstrated by pellet injection must be tempered by the presence of a subsequent phase of density decrease and by its contribution to the global discharge fuelling. In large-scale devices (ITER, DEMO), the role of pellet injection in the fuelling of the core is dominant because of the opacity of the SOL to the neutrals. But in present day mid-scale devices, the core fuelling is yet dominated by the recycling flux. For this rea-

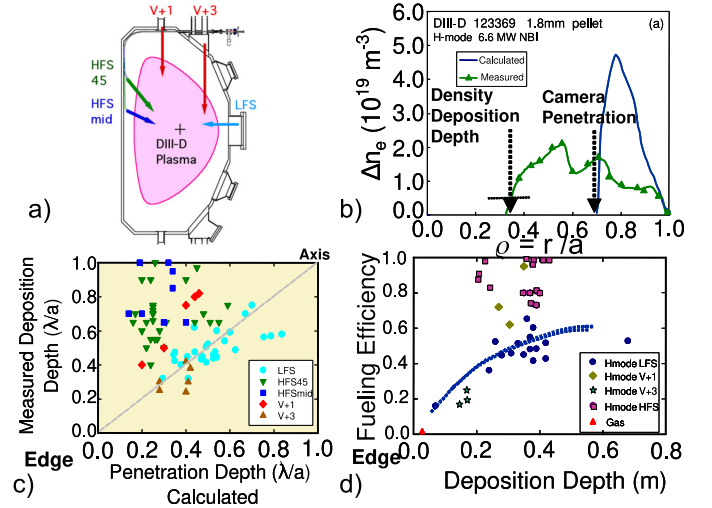


Figure 9: (a) The pellet injection locations on DIII-D mapped to a poloidal cross section. (b) Measured net pellet deposition profile from a 1.8 mm pellet injected from the inner wall (HFS-45 location) overlaid with the calculated ablation profile. (c) Measured deposition depth vs calculated pellet penetration depth for 2.7 mm pellets injected from different injection locations (Depths are normalized to the minor radius. The plasma edge is at 0.0 and the plasma center is at 1.0). (d) Fuelling efficiency of pellets injected from the different injection locations plotted as a function of the measured density deposition depth. The dashed curve is a fit to the LFS pellet data [33]

son, in Tore Supra, two macroscopically similar L-mode discharges, the former fueled by gas puff, the latter by pellet injection, demonstrated identical particle balance despite very different fueling efficiencies:  $\epsilon_f(GP) = 5\%$ ,  $\epsilon_f(PI) \sim 60\%$ , [34]. During this last decade, in tokamaks, most of the experimental activities implying pellet injection were devoted to the mitigation of disruptions using shattered pellets (like in DIII-D, KSTAR and JET), and to the demonstration of the compatibility of pellet fueling with ELM pacing by Resonant Magnetic Perturbation (RMP) in high performance scenarios (mainly in MAST and ASDEX-Upgrade). This paper concentrates on core fueling, and thus on the second of these two domains of research. The corresponding studies documented that pellet fueling was not only compatible with, but could also favor the access to H-mode ([2], see [35] for recent results), allowing to operate at a density larger than the Greenwald limit and to simultaneously control the ELMs by RMP ([2] and references therein, [36, 37, 38, 39], see an example of one of the most spectacular results in this field in Fig. 10) or by shallow pellet injection [40]. As in tokamaks, it was observed in LHD an increase in the accessible density at fixed injected power in pellet-fueled discharges [42]. However, one of the intrinsic difficulties of density control in helical devices is that, as long as the neoclassical transport dominates as expected in high performance discharges, the density profiles will be hollow in absence of deep core fueling [43]. Using pellet injection for overcoming this difficulty was extensively investigated in LHD [44] and W7-X [45]. In both cases, series of pellets (from a few to a few tens) were injected in the plasma with a high frequency (from a few tens to a few hundreds of Hz). Peaked density profiles were obtained with this technique, with a transient increase in the confinement in W7-X ([46, 47]), Fig 11, up to  $\sim 30\%$  larger than the predictions of the empirical scaling ISS04 [48]. Experiments in the superdense core mode (SDC see, e.g. [49]) were continued in LHD. This mode, which is triggered by a series of pellets in a low recycling regime, is characterized by a central core of high density and high pressure ( $5 \times 10^{20} \text{ m}^{-3}$ , 0.85 keV,  $\beta \sim 4\%$ ), stable, and maintained by an Internal Diffusion Barrier (IDB), Fig. 12. Significant MHD activity or impurity accumulation are not observed in this regime, for which end is caused by a new type of ballooning mode, localized in space, and destabilized by the 3D nature of the Heliotron configuration [50]. Pellet fueling experiments were also performed in TJ-II and Heliotron J. In TJ-II, they demonstrated the presence of a  $\nabla B$ -induced drift that lowers the fueling efficiency when the pellets are injected from the LFS, and showed that the post-pellet injection behavior was in agreement with the predictions of neoclassical theory ([51], [52]). It was also confirmed in Heliotron J that, at equivalent density, the stored energy was larger in the discharges fueled by pellets than in those fueled by gas puff [53], Fig. 13. Last, post-pellet injection transport studies were performed in the reversed field pinch RFX [54] and completed in the Madison Symmetric Torus (MST), where the Greenwald limit was overcome in a high confinement pellet-fueled discharge. In MST, the density was increased by up to a factor of 4 in discharges combining pellet fueling with pulsed poloidal current drive (PPCD), with a record in the beta value ( $\beta \sim 26\%$ ) [55].

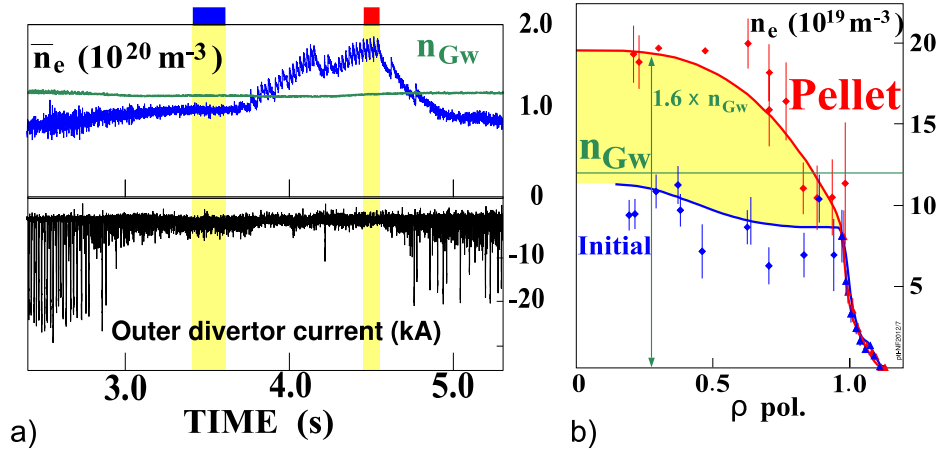


Figure 10: (a) Demonstration of RMP ELM-mitigated operation at densities far beyond the Greenwald density by pellet fueling in ASDEX-Upgrade. After reaching the mitigation regime by B-coil activation and sufficient gas puffing, maximum available pellet fueling is applied. Pellet fueling gradually increases the line-averaged density to about 1.5 times the Greenwald density without significant impact on confinement while maintaining ELM mitigation. (b) Pre- and Post-pellet density profiles (the phases for which profiles taken are indicated by vertical highlighted bars, marked by blue and red rectangles on the upper horizontal axis in a) [41].

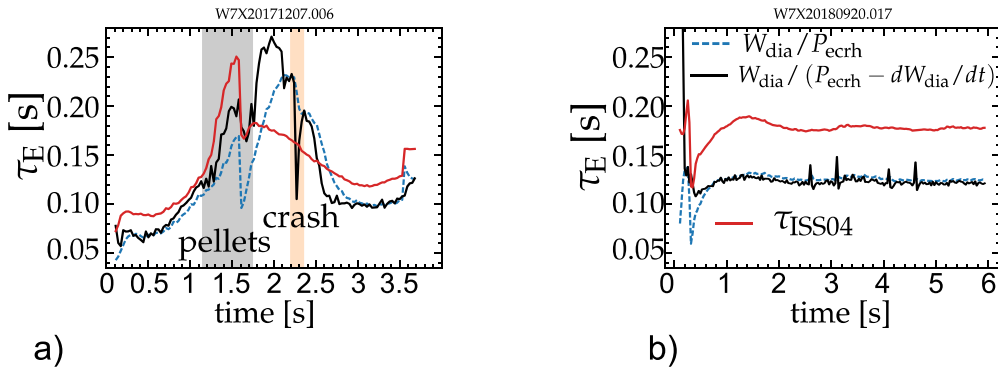


Figure 11: Comparison of the experimental global energy confinement time with the ISS04-scaling [48] for the two similar discharges in terms of average density and heating power. (a) The pellet discharge with the enhanced phase; (b) the gas-fueled discharge. Short spikes between 2 and 5 s in the gas-fueled discharge are caused by diagnostic NBI blips. For completeness, the experimental confinement time is calculated both with and without the time derivative of the diamagnetic energy. Both definitions coincide under stationary conditions. The color legend is the same for the two plots and is given in b); from [47]

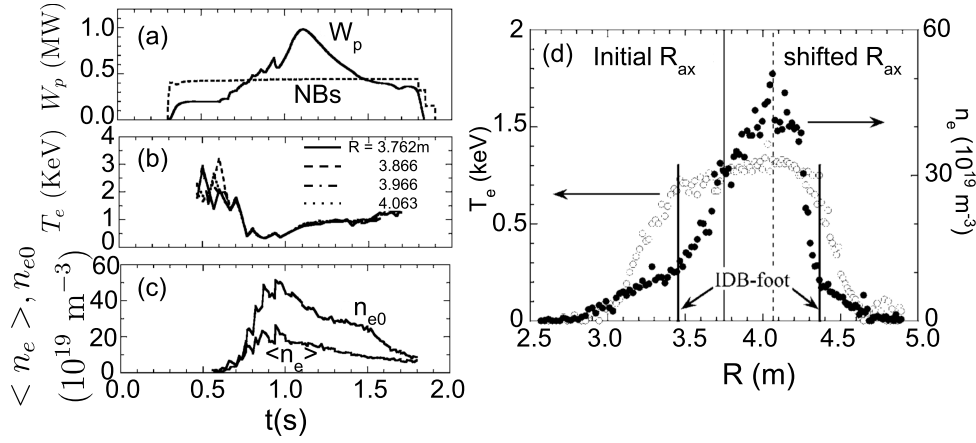


Figure 12: Time evolutions of (a) stored energy  $W_p$  together with the sequence of NBIs, (b) electron temperature  $T_e$  in the core region, and (c) central electron density  $n_{e0}$  and averaged density  $ne$  in the typical IDB-SDC mode. (d) Typical electron density (closed circles) and temperature (open circles) profiles in the IDB-SDC mode from [49].

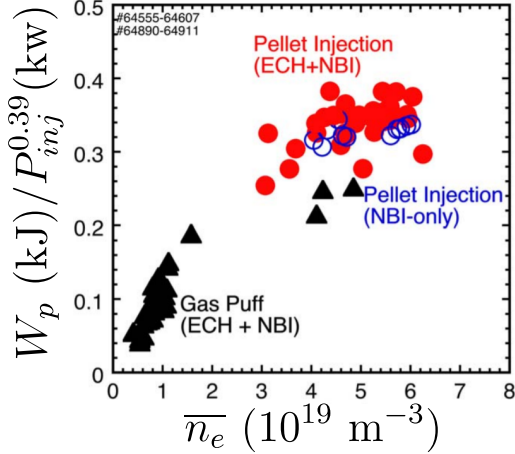


Figure 13: Normalized stored energy as a function of line-averaged electron density. The red filled symbols show the pellet shots in Neutral Beam Injection (NBI) + Electron Cyclotron Heating (ECH) plasmas. Stored energy is normalized by the heating power  $P_{inj}^{0.39}$ . Blue open circles show the pellet shots in NBI-only plasmas. The black filled triangles show the gas puff shots [53]

## 5 Fueling systems of future devices

If the experiments summarized in the previous section demonstrate that pellet injection has the capacity for fueling efficiently today's machines,

the situation will be different in the future – reactor grade – devices, and the results obtained up to now hardly extrapolated. This comes essentially from the larger plasma size and from the higher temperature and density expected at the edge of the plasma. This would result in a smaller pellet penetration (typically up to a normalized radius  $\rho = r/a \sim 0.95$  to  $0.90$ , compared to  $\rho \sim 0.7$  to  $0.5$  in present day machines). That is why drift displacement is essential to the matter penetration. Consequently, HFS pellet injection will be mandatory in both large-scale tokamaks and stellarators [56].

In fact, HFS injection is hampered by the necessity to use bended guide tubes between the pellet injector and the exit point in the vacuum chamber. This limits the injection speed because of the erosion and constraints experienced by the pellets when they slip – or bounce – along the wall of the guide tube. The maximum speed can be estimated by balancing the yield strength of the Hydrogen ice by the pressure exerted by the centrifuge force on the pellet during its path in the guide tube [57]. The resulting expression, calibrated on laboratory experiments, is  $V_p^{Max} = 36.4 [\text{m.s}^{-1}] \sqrt{R_b/2r_p}$ , where  $R_b$  is the bending radius of the guide tube. One cannot compensate this speed limitation by an increase in the pellet size, because the perturbation that results from this instantaneous density increment (pellet injec-

tion being adiabatic, the plasma is cooled in the same proportion) can induce important plasma control difficulties ([58, 59]). This is also the case when the arrival time of the pellets in the plasma is not well controlled, due e.g. to a small dispersion of the injection velocity with pneumatic injectors (gas guns). Fueling a reactor by pellet injection results therefore from a compromise between the requirement that the matter penetrates deep enough and the limitations in the pellet speed and mass mentioned above.

Presently, pellet injection systems for three large tokamaks are under manufacturing or design. By order of size and planned date of commissioning, they are those of JT-60SA, ITER and DEMO. Typical values relevant for the fueling of these machines (they can slightly change depending on the publication), with those of the FFHR project, are listed in Table 1 ([60, 61, 62, 63, 64])<sup>3</sup>.

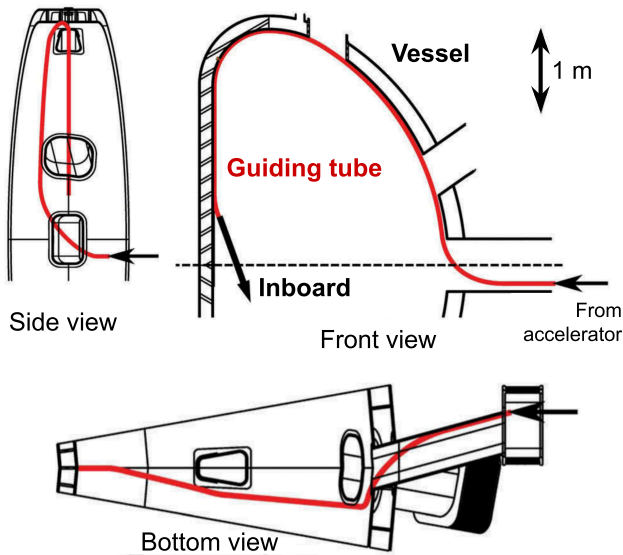


Figure 14: Guiding-tube geometry installed inside the JT-60SA vessel for pellet inboard injection. Multiple bends of the guiding tube are expected to impose a limit of about  $470 \text{ m.s}^{-1}$  to the maximum injection speed from [65].

For JT-60SA, the required fueling rate is  $\leq 30 \text{ Pa.m}^3.\text{s}^{-1}$  ( $1.5 \times 10^{22} \text{ at.s}^{-1}$ ) in Deuterium. Pellets are continuously extruded from a reservoir where the ice is formed. They have a particle

<sup>3</sup>From the author’s knowledge, no pellet fueling evaluation is available for the Chinese project CFETR.

content of  $(0.3 \text{ to } 1.3) \times 10^{21} \text{ at.}$  and are accelerated by a centrifuge injector, with a frequency up to  $50 \text{ Hz}$  [65]. The HFS injection line enters the vacuum chamber by and equatorial port, in the outer midplane, and exhibits several bends up to its end slightly above the inner midplane (Fig. 14). For reliable injection, this limits the allowed pellet speed to  $V_p^{Max} = 0.47 \text{ km.s}^{-1}$ . Simulations demonstrating the possibilities of density control with this system can be found in [60].

Concerning ITER, the expected core fueling rate is up to  $85 \text{ Pa.m}^3.\text{s}^{-1}$  ( $\sim 4.25 \times 10^{22} \text{ at.s}^{-1}$ ) [66], this value being confirmed by the simulations of the different scenarios ITER will be operated in ([67, 68]). The pellets ( $\text{H}_2$ ,  $\text{D}_2$ , 10%  $\text{D}_2 - 90\% \text{ T}_2$ ) are also continuously extruded and have a particle content of  $6 \times 10^{21} \text{ at.}$  (the plasma density increment is  $\delta n/n \sim 7\%$ ). The final system of ITER will consist in 3 pairs of injectors, each of them able to inject pellets at a maximum frequency of  $16 \text{ Hz}$ . Each pair of injectors will be equipped with 3 guide tubes (2 HFS for fueling, 1 LFS for ELM pacing, Fig. 15). In this geometry, the maximum injection speed was measured to be  $V_p^{Max} \sim 0.3 \text{ km.s}^{-1}$ , the pellets being pneumatically accelerated by a single-stage gas gun [69].

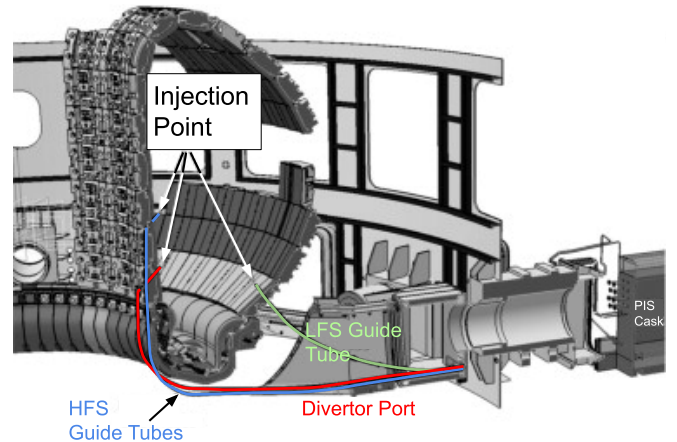


Figure 15: Geometry of the pellet injection guiding tubes on ITER via inner and outer wall guide tubes routed through a divertor port from [69].

Two versions of DEMO are being developed: one in Japan (JA-DEMO [62]), the other in Europe

	JT-60SA	ITER	JA-DEMO	EU-DEMO	FFHR-d1
R [m]	2.96	6.2	8.5	9	14.4
a [m]/ $\kappa$	1.18/193	2/1.7	2.42/1.65	2.9/1.6	2.54
$I_p$ [MA]	5.5	15	12.3	18	-
$B_\infty$ [T]	2.25	5.3	5.94	5.9	4.7
$V_{\text{plasma}}$ [m <sup>3</sup> ]	133	830	$\sim 1600$	$\sim 2400$	1878
$P_{\text{fus}}$ [GW]	-	0.5	1.42	2	3
$\langle n_e \rangle$ [ $10^{19} \text{ m}^{-3}$ ]	2 to 10	8 tot 10	6.6	7.3	$n_e(0)$ 25

Table 1: Major (R) and minor (a) radii, elongation ( $\kappa$ ), plasma current ( $I_p$ ), magnetic field ( $B_\infty$ ), plasma volume ( $V_{\text{plasma}}$ ), fusion power ( $P_{\text{fus}}$ ) and average density ( $\langle n_e \rangle$ ) for the future large devices to be operated in the next decade or in project.

(EU-DEMO [63]). For JA-DEMO, a rather complete study of the needs in terms of fueling is given in [70], the imposed constraint being that the maximum of deposition should be at  $r/a \sim 0.85$ . For the set of performed simulations, it is found that the best configuration for core fueling:

$\sim 25 \text{ Pa.m}^3.\text{s}^{-1}$  ( $\sim 1.2 \times 10^{22} \text{ at.s}^{-1}$ ), would be to inject pellets of a particle content of  $4 \times 10^{21}$  at., from HFS, with a velocity  $V_p \geq 2 \text{ km.s}^{-1}$ . Such a velocity requires to use a double-stage gas gun, the pellet being condensed *in situ* in the gun (with a condensation time  $\sim 30$  s), and large curvature radii are required for the guide tube  $R_b \sim 10$  m, Fig 16a. With these parameters, an injection frequency of 3 Hz would require to install 90 guns around the torus.

The first design of the pellet fueling system of EU-DEMO used the same pellet size as that planned for ITER ( $6 \times 10^{21}$  at.), and the first calculations of penetration / deposition profiles done in this frame [71]. However, for minimizing the difficulties in the plasma control that were resulting from a too large density increment [58], the pellet particle content was reduced down to  $2 \times 10^{21}$  at. in the pre-conceptual design [59]. The required injection frequency would be then in the range 5 to 7 Hz for an injected flux of  $\sim 20$  to  $30 \text{ Pa.m}^3.\text{s}^{-1}$  ( $\sim 1.0$  to  $1.4 \times 10^{22} \text{ at.s}^{-1}$ ). Two alternative configurations are yet considered for the injection geometry, the injector being in both cases placed above the cryostat, Figs. 16b and 16c. The first uses a curved guide tube ( $R_b \sim 10$  m), allowing an injection speed of  $V_p \sim 1.7 \text{ km.s}^{-1}$ , for which a single-stage gas gun is sufficient. The second uses

straight-line injection for minimizing the erosion in the guide tube. Pellets are then injected at high velocity ( $V_p \geq 3 \text{ km.s}^{-1}$ ) with a double-stage gas gun [72].

Presently, there is no reactor grade project of Heliotron planned to be manufactured in the next decade. Nevertheless, several studies were conducted for evaluating the fueling needs in a device of characteristics close to those of FFHR-d1 (see Table 1), of 3 GW of fusion power and of the same configuration as LHD but 4 times larger (i.e.  $\sim 60$  times in volume). Simulations were performed for evaluating the required characteristics of a fueling system (pellet size, injection speed and frequency) for satisfying the power balance in the plasma, using transport properties measured in LHD extrapolated to a thermonuclear plasma ([73, 74]). They showed that :

1. a deep core fueling is mandatory for carrying by diffusion the matter at the center of the discharge,
2. the performance of present day injectors are sufficient for the required fueling (particle content  $2 \times 10^{22}$  at, velocity  $V_p \sim 1 \text{ km.s}^{-1}$ , injection frequency 10 Hz), but at the price of a large particle throughput, of the order of  $\sim 320 \text{ Pa.m}^3.\text{s}^{-1}$  ( $1.6 \times 10^{23} \text{ at.s}^{-1}$ ),
3. it is possible to decrease this throughput by using a higher pellet speed (decrease by a factor of 3 for  $V_p \sim 10 \text{ km.s}^{-1}$ , requiring an injection frequency of  $\sim 3\text{Hz}$ ), but these velocities are out of the performance of today's technology,

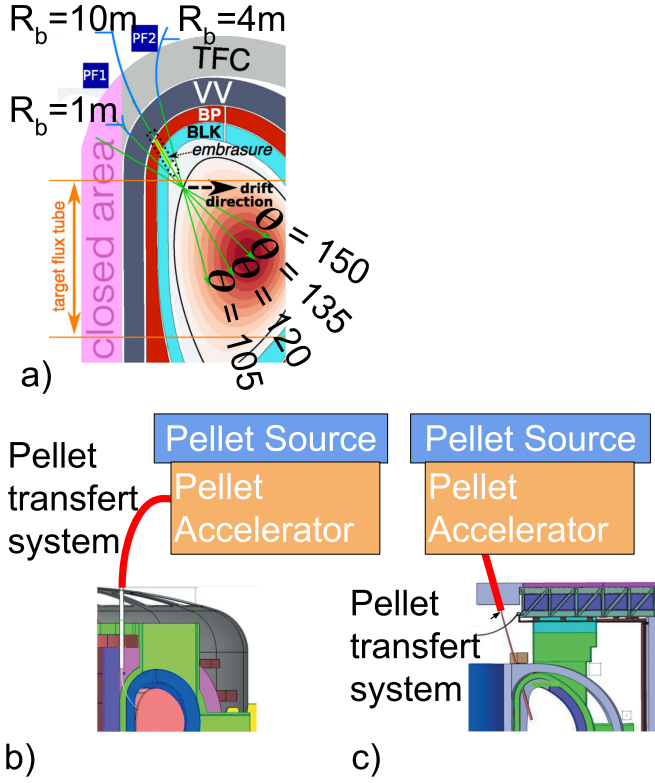


Figure 16: (a) JA-DEMO geometry including the toroidal field coils (TFC), vacuum vessel (VV), back plate (BP), tritium breeding blanket (BLK) and plasma. Spatial relationships between target flux tube and injection point, pellet guide tube curvature radius ( $R_b$ ) and injection angle ( $\theta$ ) are shown. Pink filled area is closed by TFC [70]. (b) Generic view of subsystem core fueling for EU-DEMO, composed of pellet source, pellet accelerator, and pellet transfer system aiming at the magnetic HFS of the plasma. The speed range is at least  $1200\text{ m.s}^{-1}$ , hence centrifuge or single-stage gas gun is regarded to be suitable. (c) Alternative variant using a direct-line-of-sight transfer system. High speeds up to  $3000\text{ m.s}^{-1}$  is required. Only double-stage gas gun technology will be able to reach this speed range [59]

4. it is not possible to decrease this throughput by using larger pellets, the variation of the fusion power at every injection leading to unacceptable heat loads on the divertor,
5. finally, the SDC regime, demonstrated in LHD [49], would be only accessible in a reactor if major progresses are done in the techniques of matter injection (pellet velocity larger than  $10\text{ km.s}^{-1}$  or injection of compact toroids). In this case, the fueling requirement is the same than that estimated for extrapolated LHD discharge (point 2) [75].

## 6 Summary

Up to now, pellet injection is the more mature method for a direct fueling of the plasma core in next generation devices. But the physics of the homogenization in the discharge of the matter locally deposited, under the form of cold and dense cloudlets, leads to a difference in performance depending on the type of device considered (tokamak, stellarator or reversed field pinch). A simple description of the main phenomena that – in the state of our current understanding – govern the acceleration and damping of the drift of the deposited material down the magnetic field gradient allows to explain these differences. Particularly, one shows that, everything else being equal, the material radial displacement during its homogenization is larger in a tokamak than in a stellarator, and that its drift is mainly damped close to the reversal radius in a reversed field pinch. The two main advantages of pellet injection w.r.t. the other usual fueling methods (Gas Puff and Supersonic Molecular Beam Injection), namely a higher fueling efficiency and a better decoupling between the core and edge densities, are documented for a long time. Consequently, activity during this last decade was more concentrated on the compatibility of pellet fueling with the high performance plasma scenarios envisaged in the future machines. In tokamaks, in addition to the experiments on the mitigation of disruptions with shattered pellets, the main progress

was, in ASDEX-Upgrade, the demonstration that pellet fueling could be compatible with the suppression of ELMs by Resonant Magnetic Perturbation in discharges of density larger than the Greenwald limit. In helical devices, the density profile tends to be hollow when the neoclassical transport is dominant. This difficulty was overcome in LHD and W7-X by the injection of trains of pellets at high frequency, the cooling of the plasma by the first pellets allowing the others to penetrate deeper in the discharge. This technique made possible not only to obtain peaked density profiles, but also led to an energy confinement larger than that predicted by the empirical scaling ISS04. A better confinement was also measured in Heliotron J in pellet fueled discharges. These good results are nevertheless difficult to extrapolate to the next generation devices, of larger size, where the pellet material deposition will be shallow.

In these future machines, where the plasma pressure will be higher, the presence of the  $\nabla B$ -induced drift will impose to inject pellets from the High Field Side. If high velocity injection from the top of the device – which requires a rectilinear guide tube – remains an option for EU-DEMO, the other projects (JA-DEMO, ITER, JT-60SA) privilege pure High Field Side injection with bended guide tubes, even if the latter strongly limit the injection velocity. This point underlines how it is important to integrate the pellet injection system from the beginning of the design of a device for minimizing the speed limitation. If in future tokamaks a deep enough deposition depth can be obtained with present injector technology, this is not the case in reactor-grade stellarators, where the first simulations tend to indicate that the required velocities are of the order or higher than  $10 \text{ km.s}^{-1}$ . A last point to be noted is – and this is the case for all the pulsed techniques of matter injection – that every pellet induces a variation of the instantaneous fusion power and of the heat load on the divertor. The pellet particle content must consequently be small in front of that of the plasma for this perturbation does not lead to difficulties in the plasma control and to preserve the integrity of the most exposed Plasma Facing

Components.

## Acknowledgment

This work has been carried out within the framework of the EUROfusion Consortium and has received funding from the European research and training programme 2014-2018 and 2019-2020 under grant agreement N° 633053. The views and opinions expressed herein do not necessarily reflect those of the European Commission.

## References

- [1] M. Romanelli et al. In: *Nucl, Fusion* 55 (2015), p. 093008.
- [2] B. Pégourié et al. In: *Plasma Phys. Control. Fusion* 49 (2007), R87.
- [3] B. Pégourié et al. In: *Plasma Phys. Control. Fusion* 51 (2009), p. 124023.
- [4] S.K. Combs and L.R. Baylor. In: *Fusion Sci. Technol.* 73 (2018), p. 493.
- [5] R. Raman. In: *Fus. Eng. Des.* 83 (2008), p. 1368.
- [6] W.A. Houlberg et al. In: *Nucl, Fusion.* 28 (1988), p. 595.
- [7] N. Bosviel et al. In: *Phys.plasma* 28 (2021), p. 012506.
- [8] R. Samulyak et al. In: *Nucl, Fusion.* 61 (2021), p. 046007.
- [9] V.A. Rozhansky and I.Yu. Senichenkov. In: *Plasma Phys. Rep.* 31 (2005), p. 993.
- [10] Y. Nakamura et al. In: *Nucl, Fusion.* 32 (1992), p. 2229.
- [11] B. Pégourié et al. In: *Plasma Phys. Control. Fusion* 47 (2005), p. 17.
- [12] A. Matsuyama et al. In: *Plasma Phys. Control. Fusion* 54 (2012), p. 035007.
- [13] A. Bortolon et al. In: *Nucl, Fusion.* 59 (2019), p. 084003.
- [14] K.J. McCarthy et al. In: *Plasma Phys. Control. Fusion* 61 (2019), p. 014013.
- [15] A.M. Arnold et al. In: *Plasma Phys. Control. Fusion* 63 (2021), p. 095008.
- [16] V.A. Rozhansky et al. In: *Plasma Phys. Control. Fusion* 37 (1995), p. 399.
- [17] P.B. Parks and L.R. Baylor. In: *Phys. Rev. Lett.* 94 (2005), p. 125002.
- [18] P.B. Parks et al. In: *Phys.plasma* 7 (2000), p. 1968.
- [19] B. Pégourié et al. In: *Nucl, Fusion* 47 (2007), p. 44.
- [20] V.A. Rozhansky et al. In: *Plasma Phys. Control. Fusion* 46 (2004), p. 575.
- [21] A. Matsuyama et al. In: *Nucl, Fusion.* 52 (2012), p. 123017.
- [22] R. Ishizaki and N. Nakajima. In: *Plasma Phys. Control. Fusion* 53 (2011), p. 054009.
- [23] R. Sakamoto et al. In: *Nucl, Fusion.* 53 (2013), p. 063007.
- [24] A. Canton et al. In: *Plasma Phys. Control. Fusion* 43 (2001), p. 225.
- [25] A. R. Polevoi and M. Shimada. In: *Plasma Phys. Control. Fusion* 43 (2001), p. 1525.
- [26] F. Köchl et al. In: *Prepr. EFDA-JET-PR(12)* 57 (2012), p. 82.
- [27] N. Panadero et al. In: *ECA-43C* (2019), P1.1077.
- [28] L. Garzotti et al. In: *Nucl, Fusion.* 50 (2010), p. 100502.
- [29] N. Commaux et al. In: *Nucl, Fusion.* 50 (2010), p. 025011.
- [30] N. Hayashi et al. In: *Nucl, Fusion.* 51 (2011), p. 103030.
- [31] N. Panadero et al. In: *Nucl, Fusion.* 58 (2018), p. 026025.
- [32] B. Pégourié et al. In: *J. Nucl. Mater.* 313-316 (2003), p. 539.
- [33] L.R. Baylor et al. In: *Nucl, Fusion.* 47 (2007), p. 1598.
- [34] A. Géraud et al. In: *J. Nucl. Mater.* 337-339 (2005), p. 485.
- [35] M. Valovic et al. In: *Nucl, Fusion.* 52 (2012), p. 114022.
- [36] M. Valovic et al. In: *Nucl, Fusion.* 55 (2015), p. 013011.
- [37] P.T. Lang et al. In: *Nucl, Fusion.* 52 (2012), p. 023017.
- [38] M. Valovic et al. In: *Plasma Phys. Control. Fusion* 60 (2018), p. 085013.
- [39] M. Valovic et al. In: *Nucl, Fusion.* 60 (2020), p. 054006.
- [40] P.T. Lang et al. In: *Nucl, Fusion.* 54 (2014), p. 083009.
- [41] P.T. Lang et al. In: *Nucl, Fusion.* 52 (2012), p. 023017.

- [42] R. Sakamoto et al. In: *Nucl, Fusion*. 41 (2001), p. 381.
- [43] C.D. Beidler et al. In: *Plasma Phys. Control. Fusion* 60 (2018), p. 105008.
- [44] J. Baldzuhn et al. In: *Plasma Phys. Control. Fusion* 60 (2018), p. 035006.
- [45] J. Baldzuhn et al. In: *Plasma Phys. Control. Fusion* 61 (2019), p. 095012.
- [46] J. Baldzuhn et al. In: *Plasma Phys. Control. Fusion* 62 (2020), p. 055012.
- [47] S.A. Bozhnikov et al. In: *Nucl, Fusion*. 60 (2020), p. 066011.
- [48] H. Yamada et al. In: *Nucl, Fusion*. 45 (2005), p. 1684.
- [49] T. Morisaki et al. In: *Phys. Plasmas* 14 (2007), p. 056113.
- [50] S. Ohdachi et al. In: *Nucl, Fusion*. 57 (2017), p. 066042.
- [51] K.J. McCarthy et al. In: *Nucl. Fusion* 57 (2017), p. 056039.
- [52] J.L. Velasco et al. In: *Plasma Phys. Control. Fusion* 58 (2016), p. 084004.
- [53] G. Motojima et al. In: *Plasma Phys. Control. Fusion* 61 (2019), p. 075014.
- [54] R. Lorenzini et al. In: *Plasma Phys. Control. Fusion* 44 (2002), p. 233.
- [55] M. D. Wyman et al. In: *Nucl. Fusion* 49 (2009), p. 015003.
- [56] B. Pégourié et al. In: *ECA-40A* (2017), p. 4.076.
- [57] P.T. Lang et al. In: *Fusion Eng. Des.* 96-97 (2015), p. 123.
- [58] F. Janky et al. In: *DEMO Control Challenges 31st SOFT* (2020).
- [59] B. Ploeckl et al. In: *Fusion Sci. Technol.* 77 (2021), p. 266.
- [60] G. Giruzzi et al. In: *Plasma Phys. Control. Fusion* 62 (2020), p. 014009.
- [61] M. Shimada et al. In: *Nucl. Fusion* 47 (2007), S1.
- [62] K. Tobita et al. In: *Fusion Sci. Technol.* 75 (2019), p. 372.
- [63] G. Federici et al. In: *Nucl. Fusion* 59 (2019), p. 066013.
- [64] A. Sagara et al. In: *Fusion Eng. Des.* 87 (2012), p. 594.
- [65] P. T. Lang et al. In: *Fusion Sci. Technol.* 75 (2019), p. 178.
- [66] A.S. Kukushkin et al. In: *J. Nucl. Mat.* 415 (2011), p. 5497.
- [67] L. Garzotti et al. In: *Nucl, Fusion*. 52 (2012), p. 013002.
- [68] F. Koechl et al. In: *Nucl, Fusion*. 60 (2020), p. 066015.
- [69] S. K. Combs et al. In: *Fusion Eng. Des.* 87 (2012), p. 634.
- [70] S. Tokugana et al. In: *Fusion Eng. Des.* 123 (2017), p. 620.
- [71] P. Vincenzi et al. In: *Nucl. Fusion* 55 (2015), p. 113028.
- [72] A. Frattolillo et al. In: *Fusion Eng. Des.* 162 (2021), p. 112138.
- [73] R. Sakamoto and H. Yamada. In: *IEEE Transactions on Plasma Science* 44 (2016), p. 2915.
- [74] T. Goto et al. In: *Fusion Eng. Des.* 89 (2014), p. 2451.
- [75] R. Sakamoto and H. Yamada. In: *Fusion Eng. Des.* 89 (2014), p. 812.